Charge transport in single crystal CVD diamond studied at high temperatures

Andreo Crnjac[1,*], Mauricio R. Ramos[1], Natko Skukan[1,†], Michal Pomorski[2] and Milko Jakšić[1],

[1] *Division of Experimental Physics, Ruđer Bošković Institute, 10000 Zagreb, Croatia*
[2] *Université Paris-Saclay, CEA, List, F-91120 Palaiseau, France*

* acrnjac@irb.hr
† Presently on long term leave to the International Atomic Energy Agency.

Abstract

The capability of single crystal diamonds to maintain their unique electronic properties even at high temperatures is, in particular, relevant for its applications as a radiation detector. In order to explore characteristics of charge transport at high temperatures (up to 450 °C), diamond was exposed to MeV energy ions, both, to induce radiation damage and to probe subsequent influence on detector's properties. Dependence of mobility-lifetime product with temperature has been obtained for electrons and holes. For holes, mu-tau displays a linear degradation with rising temperature, while for electrons, change with temperature is less evident. Furthermore, deep trapping levels induced in the material by radiation damage, were studied through time-resolved charge signals. Detrapping time was extracted from this data. Hole trap level, with the activation energy of 0.53 ± 0.01 eV has been detected in the regions of the diamond detector previously irradiated by 5 MeV damaging proton beam, but not in the pristine regions. This indicates that the trap was formed due to defect induction during radiation damage exposure. Activation of this deep level is important for charge transport performance in diamond detectors operating at high temperatures and high radiation conditions.

Keywords: diamond detector, charge transport, radiation damage, high temperature, detrapping

1 Introduction

Employment of diamond for radiation detection, power electronics and optoelectronics has been increasing steadily in the last two decades. Constant developments in synthesis processes [1] have resulted in high purity synthetic diamond crystals becoming readily available on the market. Larger substrate sizes are also becoming more common [2]. Diamond is an ultra-wide-band-gap semiconductor (5.5 eV) with excellent properties: breakdown voltage >10 MV/cm, high electron and hole mobilities, chemical inertness, radiation hardness, high thermal conductivity [3].

Based on these properties, diamond-based radiation detectors have found increasing use for operation in harsh environments, specifically high radiation and/or high temperature conditions, that can be encountered at nuclear fusion reactors or other

nuclear or particle physics experimental facilities [4–6]. Devices for power and high frequency electronics are also being actively developed [7]. High thermal conductivity is here especially important for heat dissipation, as it was demonstrated for diamond-based JFET [8] that was able to operate at temperatures up to 450 °C.

However, regarding diamond radiation detector's performance at elevated temperatures, several authors have reported inconclusive results for the electronic performance of their devices [6, 9–13]. Significant leakage current and signal degradation have been observed at temperatures higher than room temperature (RT). In some cases this degradation starts already at 100 °C, and renders a device not operational. [13]. Free charge carrier density for an intrinsic diamond at room temperature is extremely low and can be estimated as $n_i \sim 10^{-27}\,\mathrm{cm}^{-3}$. It increases with rising temperature to $n_i \sim 10^{-18}\,\mathrm{cm}^{-3}$ at 100 °C, and further goes $n_i \sim 10\,\mathrm{cm}^{-3}$ at 500 °C [14]. Altogether, these values still give a negligible number of free carriers in a typical detector device volume . This indicates that those high temperatures for perfect diamond crystals should not impact macroscopic properties (such as leakage current) noticeably. It can be concluded that free carrier density at higher temperatures will be dictated by presence of impurities, which determine the crystal quality.

We surmise that the inconsistencies in the reported high-temperature behaviour arise mainly due to sample quality variation, as well as poor thermal resilience of the electronic processing components exposed to elevated temperatures on the detector mount. The latter impairs the possibility to separate the temperature effect occurring in and outside the diamond itself. In a recent work [15] we have investigated spectroscopic properties of a radiation detector, based on a single crystal CVD diamond, specifically prepared for high-temperature operation. The device was able to maintain an almost constant energy response up to 450 °C. However, radiation hardness testing showed that Charge Collection Efficiency (CCE) from regions previously exposed to MeV proton beam radiation damage deteriorated with rising temperature. The decreasing trend was stopped at around 380 °C, after which saturation and even signal amplitude recovery was observed.

This overall decrease of the collected charge could be correlated with degradation of mobility of electrons and holes with rising temperature [7], which leads to increased trapping probability [16].

In this work, we have attempted to further investigate the charge transport performance of diamond radiation detectors, during exposure to high radiation and high-temperature conditions. Ion beam techniques were used to induce charge signal in both radiation-damaged and pristine regions of the device. First, mobility-lifetime product for both electrons and holes was studied as a function of temperature. Next, to monitor thermally activated emission of carriers from trapping centres induced in sample by ion irradiation, charge transient pulses were recorded. Temporal analysis of the acquired data enables the identification of the deep trap activation energy.

2 Experimental setup

A single-crystal Chemical Vapor Deposition (sc-CVD) high purity diamond ([N] $<$ 5 ppb, [B] $<$ 1 ppb), produced by Element Six Ltd. [17], with <100> crystal orientation and 65 um thickness, was used to create a radiation detector with planar geometry. After the deposition of tungsten electrodes, the detector has been mounted on a housing specially designed for the operation at high temperatures. Details about this detector construction were described in our previous work [15]. One side of the detector remained opened for exposure by probing or damaging radiation, which were in this case MeV energy range ions. To characterize the detector, we have employed experimental techniques based on the ion beams. Detector was mounted in the ion microprobe setup

attached to the 1 MV Tandetron accelerator at the Ruđer Bošković Institute [18, 19]. The backside of the detector mount was in constant direct contact with a resistive heater, connected to a temperature controller. The front side was exposed to the ion beam, so that ions penetrate the top electrode in the direction of the applied electric field through the detector. Figure 1 displays schematically this geometry and the experimental setup. The microprobe system enables the focusing of the ion beam to a

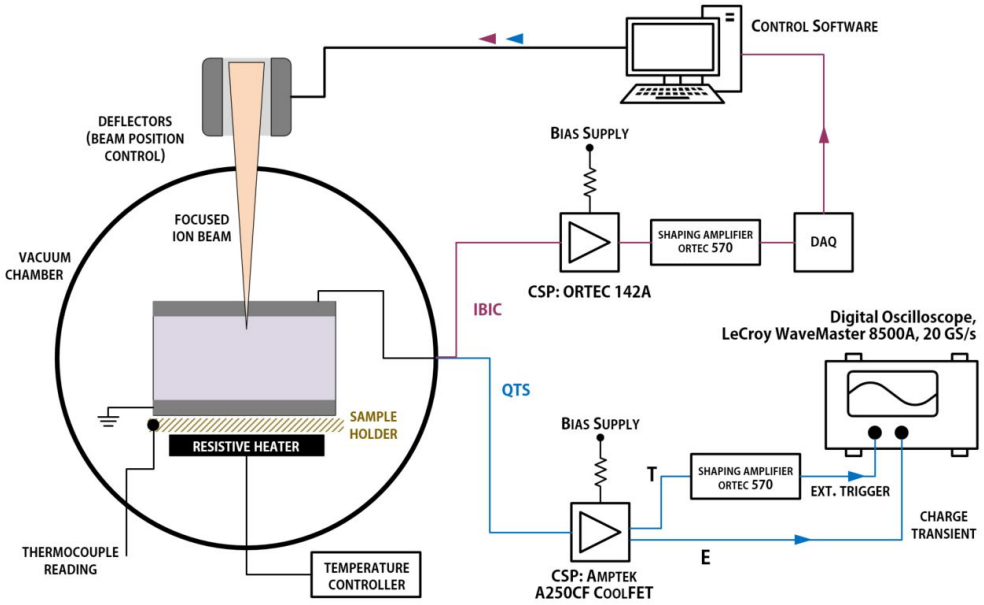

Figure 1. Schematic representation of the experimental setup in the ion microprobe vacuum chamber, as well as electronic chains for IBIC and QTS signal processing and collection. Detector is exposed to focused ion beams from the top electrode. The same electrode is used to supply bias voltage and to read the signal response from the detector, while the bottom electrode is grounded. For the QTS technique, timing output (T) from the A250CF preamplifier was acting as a trigger event at the oscilloscope for saving of charge transients coming through the energy (E) line.

micrometre spot, while two electromagnetic dipoles, computer-controlled by the in-house developed software SPECTOR-v2 [20], provide scanning capability over the selected regions of the sample. In our case, this setup was used for spatial mapping of the signal induced by ions. More specifically, two experimental techniques were used: Ion Beam Induced Charge (IBIC) [21], where the detector's charge pulses are integrated and pulse height analysis is performed; and Charge Transient Spectroscopy (QTS) [22, 23], where the time structure of the charge pulse is preserved and analyzed. Mobility-Lifetime informations were extracted from the IBIC measurements, while QTS data was used to observe thermally induced charge detrapping effects. The schematic representation of the experimental conditions for both techniques is displayed in figure 1.

For the QTS characterization, the charge traces were amplified using a charge sensitive preamplifier (CSP), Amptek A250CF CoolFET, connected to a digital oscilloscope, Lecroy WaveMaster 8500A. For the data analysis, signals were stored in the integrated oscilloscope memory drive, and offline analysis and fitting were performed (procedure details are explained in the section 3). During the performance of conventional IBIC characterization, detector response, induced by the ion beam, was amplified through the ORTEC 142A CSP and further shaped with ORTEC 570 amplifier, with 0.5 µs shaping time constant. A multichannel analyzer was used for pulse height spectra acquisition. Finally, data were transferred to the personal computer

for online processing and analysis. Electronic chain was calibrated by comparison with silicon surface barrier detector, with estimated 100% CCE, and a pulse generator. Energy for e-h pair creation of 3.62 eV [24] in Silicon and 13 eV in diamond [25] was assumed.

To test the influence of radiation damage on the charge transport at high temperatures in diamond, a small section of the detector was previously exposed to the 5 MeV damaging proton beam. Radiation damage was introduced at room temperature. 5 MeV protons penetrate the full thickness of the detector, and deposit an almost uniform profile of point defects in the crystal lattice. Fluence deposited in the 100×100 μm^2 damaged region was $1.5 \cdot 10^{13}\,cm^{-2}$, with induced vacancy density $4.4 \cdot 10^{13}\,cm^{-3}$, as calculated with SRIM [26].

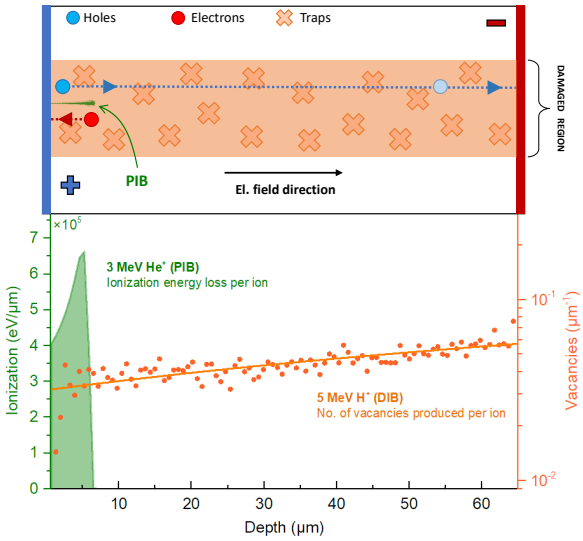

Figure 2. *Lower panel:* Ionization profile of 3 MeV He^+ ions, used as probes for inducing charge signal in the detector (Probing Ion Beam = PIB), and vacancy profile (together with linear fit - solid orange line) for 5 MeV H^+ ion beam used to for radiation damage introduction (Damaging Ion Beam = DIB). *Upper panel:* Schematic depiction of the detector volume exposed to radiation damage, as seen from the side, between electrodes. After irradiation with the DIB, traps are formed in the damaged region. Charge created afterwards with the PIB, can be trapped during drift in the electric field applied through electrodes.

In all further probing cycles for either IBIC or QTS, a 3 MeV He^+ beam was used. The typical event rate registered at the detector was around 50 cps during the QTS charge trace acquisition, and 1 kcps during the IBIC collection. In figure 2 (lower panel) we can see the ionization profile of 3 MeV He^+ ions probing ion beam, as well as the vacancy profile for 5 MeV protons (damaging ion beam). It is visible that all of the charge induced by the probing ions is in the first 5.8 μm of depth, which is less than 10% of the thickness between electrodes. Charge drifting to the opposite electrode will therefore dominantly contribute to the collected signal, and in this way, we can easily distinguish between electron and hole properties. For the signals collected during ion beam impinging in the damaged region, the trapping can occur during the whole charge carrier transit, because all of the path is populated with defects induced by previous irradiation with 5 MeV proton beam. This is also depicted schematically in the upper panel of figure 2. Accumulated ion dose during these probing cycles was insignificant and did not influence device performance in the sense of noticeable radiation damage creation or buildup of local electric field due to polarization effect [27, 28].

3 Results and discussion

3.1 Charge Transient Spectroscopy (QTS)

Figure 3 displays a typical IBIC map, collected by the 3 MeV He^+ ion beam that was scanned over the particular detector area. We used information from the map to locate damaged and pristine regions of the detector.

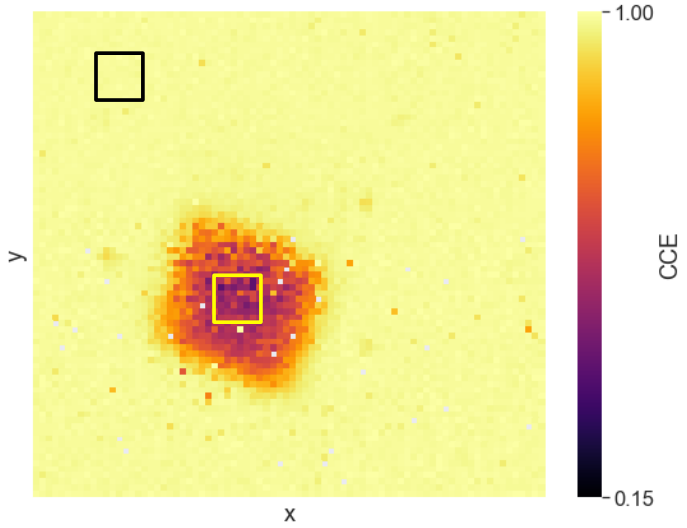

Figure 3. IBIC map collected during beam scanning over the previously irradiated region in the diamond detector. Color represents CCE. To characterize CCE in the pristine or damaged region, only data from within black or yellow square area was extracted. Damaged region has a 100×100 µm^2 size. This map was acquired at room temperature conditions.

For the study of the thermally stimulated detrapping, we acquired charge transients induced by the ion beam, that was positioned either in the central part of the previously irradiated region, or in the pristine area. In this way, we tried to distinguish possible differences between the influences of the radiation-induced defects and defects already present in the crystal lattice. Several hundred charge transients induced by shallow ion injection were recorded for each of the regions. By applying positive or negative bias to the front electrode (± 15 V), direction of the electric field was varied, and either electron or hole drift was generating the signal.The procedure was repeated for various increasing temperatures, from room temperature (23 °C) to 450 °C.

To extract detrapping time constant from the acquired signals, we need to model and quantify the transient behaviour of the induced charge. Since diamond can be considered as an ionization chamber, the electric field has a constant value everywhere between the electrodes. Let us first consider a current signal response in the diamond with trapping centers present in the crystal lattice. Charge trapping would induce an exponential decay of the current signal $I \propto \exp(-t/\tau_D)$, where τ_D is a detrapping time constant [29]. Without trapping, all of the charge is induced and collected in the carrier's transit time window. For reference, one can expect a transit time shorter than 2 ns for electron drift in a 100 µm diamond thickness, under standard electric fields of ≤ 1 V/µm. Detrapping effect will result in a delayed transport of charge, longer than the average transit window. Since charge is only a time integral of current, it can be demonstrated that the charge response of the detector would consist of two components: $Q(t) = Q_{\text{fast}} + Q_{\text{slow}}\,(1 - \exp(-t/\tau_D))$. The fast component corresponds to the charge collected during the transit time window so that detrapping effect is only present in the

slow component. After enough time all the charge would be detrapped and $Q(t \gg \tau_D) = Q_{\text{fast}} + Q_{\text{slow}}$. Plotting the $Q(t \gg \tau_D) - Q(t)$ will result in:

$$Q(t \gg \tau_D) - Q(t) = Q_{\text{slow}} \exp(-t/\tau_D), \tag{1}$$

and appropriate exponential fitting will retrieve a detrapping time constant from the transient. This approach to QTS data analysis has been applied successfully in trap relaxation time evaluation using charge transients induced by ions, in several previously published works [29, 30]. Averaged transient waveforms for electrons and holes, recorded

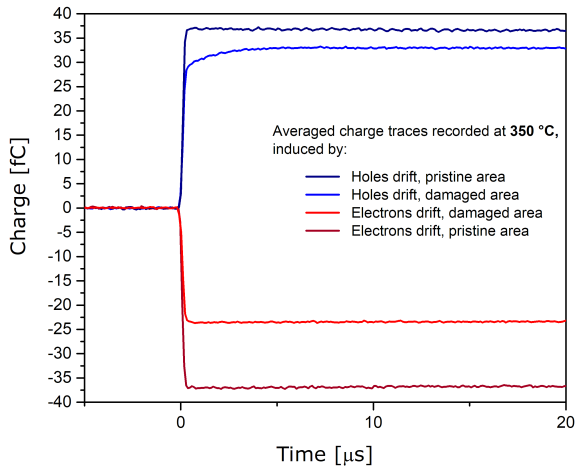

Figure 4. Averaged waveforms recorded at 350 °C, induced due to hole or electron drift in damaged and undamaged detector areas. Charge deficiency is observed in damaged regions for both types of charge carriers. Hole detrapping is also visible for the signal induced in the damaged region.

at 350 °C, are plotted together in figure 4. Amplitudes of the signals in damaged regions are lower than in pristine regions, for both types of charge carriers, revealing an incomplete charge collection. However, only the signal induced by hole drift exhibited a detrapping effect. The slow component in hole transients was observed for all temperatures above 200 °C. Trap relaxation was recorded only in the damaged region. Moreover, no detrapping effect was recorded for electron transients, indicating that the trap responsible for this effect only captured and released holes. Regarding electron collection, due to lower CCE in the damaged region, as compared to pristine, it can be concluded that electrons are also being trapped. Higher temperatures are probably needed to thermally induce electron releasing. To extract hole detrapping time, around hundred traces were acquired for each of the eight temperature points in the range from 200 °C to 450 °C (highest covered temperature). Two individual waveforms related to the same dataset, collected at 275 °C, are displayed in figure 5. It is visible that the delayed charge transport (slow component) is only present in one of these traces. It has to be noted that fast traces were present in all of the datasets, recorded at different temperatures, however, transients with slow component were dominating. Similarly, the occurrence of both transient types was reported before in the experiment with charge traces acquisition induced by alpha source irradiation of the sc-CVD diamond [30]. The explanation for the signals without the slow component is unclear, but they probably originate from the defect free detector areas.

Out of each dataset we have selected only the transients with the characteristic slow component, between 20 and 40 traces, that have been averaged. Fitting was performed

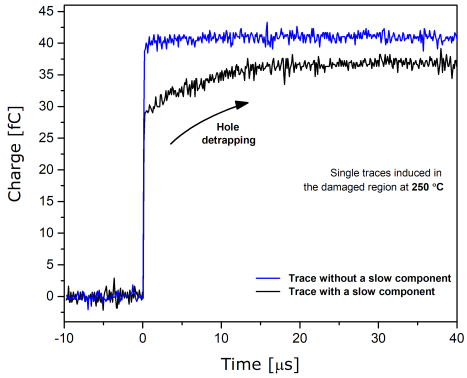

Figure 5. Two transients induced by the hole drift in the radiation damaged diamond region at 250 °C. In one of the traces (black) there is a characteristic detrapping effect, while in the other one (blue), there is no slow component. Similarly, in all datasets (for different temperatures) both types of transients were present.

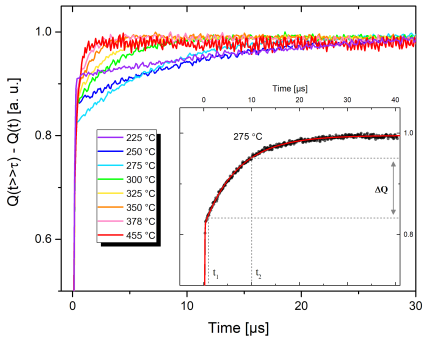

Figure 6. Signals measured from the charge preamplifier, normalized to [0, 1] interval. In the inset, one of the traces is isolated and displayed together with the fitting function according to equation 2 (red line). Also, in the inset we have indicated the procedure of extracting the ΔQ value, as a charge difference in two time points, t_1 and t_2.

on the averaged waveforms, according to the equation (1). The evolution of charge traces recorded in the temperature range between 225 °C and 455 °C are shown in figure 6 while in the inset, one of the traces was isolated and shown together with the fitting result. To estimate at which temperature is detrapping process most active, one can plot the difference between the values of the charge amplitude (ΔQ) observed at two different transient times, for example at 1 μs and 10 μs (visually explained in the inset of the figure 6). ΔQ distribution is displayed in figure 7 and demonstrates a maximum of charge detrapping rate at 275 °C.

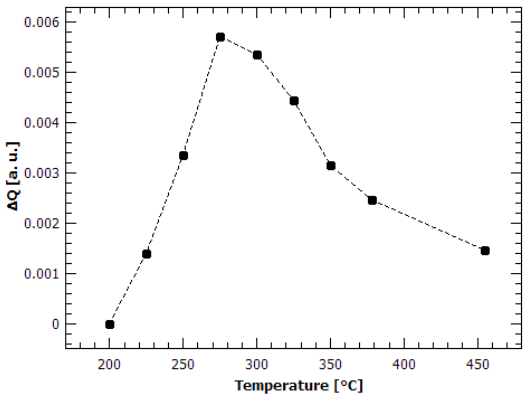

Figure 7. Difference of the charge pulse amplitude measured in a time window of $t_2 = 10$ μs and $t_1 = 1$ μs. This plot is sometimes referred to as QTS spectrum. Peak position, or maximum charge amplitude difference, is observed at 275 °C.

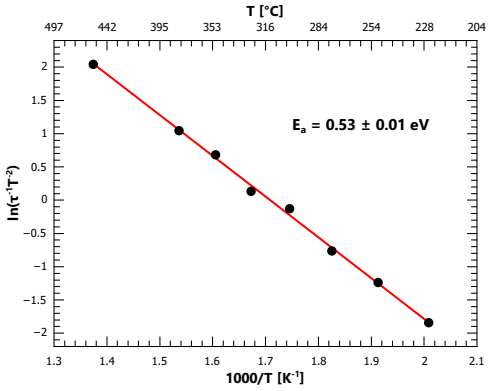

Figure 8. The Arrhenius plot for the detrapping time constant: logarithm of the $1/\tau T^2$ as a function of the inverse absolute temperature. Slope of the linear approximation line yields $-E_a/k_B$.

Based on the Shockley-Read-Hall statistics of the exchange of carriers between the bandgap levels and the band [23, 31], we know that the average detrapping time (for

electrons or holes) is related to the trap energy level:

$$\tau_D^{-1} = \sigma\,\Gamma\,T^2\exp(-E_a/k_BT), \tag{2}$$

where σ is trap capture cross-section, emission rate for electrons (holes) $\Gamma_{e(h)} = 2\sqrt{3}\,\left(2\pi/h^2\right)^{\frac{3}{2}}\,k_B^2\,m^*_{e(h)}$ (with $m^*_{e(h)}$ being the effective mass of the charge carrier), and E_a is the trap activation energy. Measuring trap relaxation time for different temperatures thus enables extraction of both activation energy and capture cross section of the trap level.

From the above data and following the equation (2), trap relaxation times were used to produce an Arrhenius plot, figure 8. Linear fitting to the data yielded following information: the activation energy $E_a = 0.53 \pm 0.01$ eV (from the slope of the linear fit); and the capture cross-section $\sigma = (2.42 \pm 0.05) \cdot 10^{-17}$ cm^2 (from the intercept parameter). For the cross-section calculation, it was assumed that the hole conductivity effective mass (needed for the emission rate evaluation) is $m^*_h = 0.46\,m_0$ [25]. Since this is not the only possible value to be considered (see, for example, [32] for more information and recent measurements) the cross-section value should be taken only as the order of magnitude indicator.

Deep trap with the similar activation energy as identified in these measurements has been observed before in unintentionally doped HPHT type IIa and Ib diamond [33], in B-doped polycrystalline CVD diamonds [34], as well as in neutron irradiated scCVD diamond [35]. The origin of the defect has not been determined decisively. 5 MeV protons primarily induce point defects, namely vacancies (V) and interstitials (I). Since V become significantly mobile only at temperatures above 600 °C in diamond [36], it is likely that this defect is I related center.

It must be stressed again that we have not detected detrapping from this level in un-irradiated diamond regions, indicating that the proton beam irradiation induced the formation of the observed capture center Charge release from this center at temperatures above 200 °C could be an important finding for diamond-based solid-state devices operating at elevated temperatures. As we have previously reported [15], diamond detector irradiated with MeV protons experienced collection efficiency decrease with elevated temperatures, but this drop was saturated at 380 C, after which recovery of CCE has been observed. Identification of the hole trap relaxation presented in this work corresponds well with the previous findings, as detrapped holes can contribute to the collected charge. This indicates that the diamond-based radiation detectors operating in high-temperature and high-radiation conditions can experience beneficial signal recovery after full settlement of this trapping center (probably not far above 450 °C).

3.2 Mobility-lifetime measurements

To measure mobility-lifetime product, we extracted pulse height spectra from the IBIC scans of the pristine area (black square area in figure 3) collected at different applied electric fields. These data should behave according to the Hecht equation [37]:

$$CCE = Q_{\mathrm{ind}}/Q_{\mathrm{total}} = \mu\tau\,\frac{E}{d}\cdot\left[1-\exp\left(\frac{x-d}{\mu\tau\,E}\right)\right], \tag{3}$$

where E is the applied electric field, x is the penetration depth of the e-h pairs inducing short-range particle, d is the distance between electrodes and $\mu\tau$ is the mobility-lifetime product (fitting parameter) of the dominant charge carrier. We have measured this dependency for both electrons and holes, in the temperature range from room temperature to 450 °C. Several data sets are displayed in figure 9, together with the fitting functions, while in the table 1 all of the fitting results are listed, together with R^2 goodness-of-fit values (see table description for details).

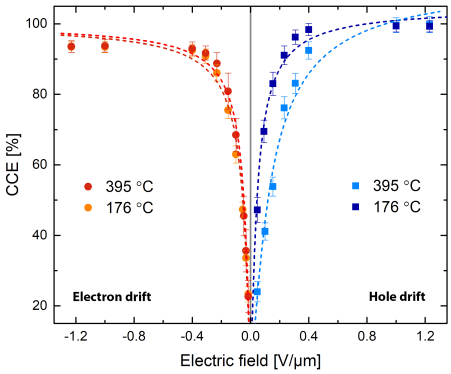

Figure 9. CCE for different electric fields, collected at two elevated temperatures, 176 °C and 395 °C, for both hole and electron drift. Together with the data are plotted fits (dashed lines) according to the Hecht equation 3.

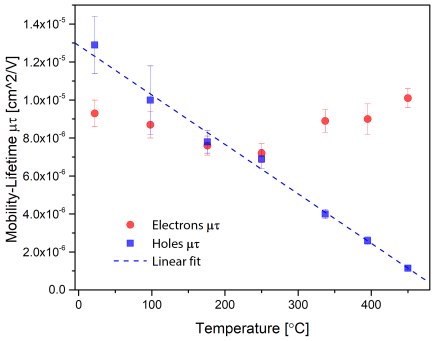

Figure 10. Mobility-Lifetime product for electrons and holes as a function of temperature. $\mu\tau$ was obtained as a fitting parameter of the Hecht equation 3. Clear decreasing trend is visible for holes, with rate of change: $-2.6 \cdot 10^{-8}\,(cm^2/V)/°C$. For electrons, trend is bi-modal, initial decrease is stopped and reversed above 250 °C.

Results demonstrate that the data are indeed reasonably well represented by the Hecht formula, with lowest R^2 value being 0.97. It should be repeated that product was here obtained indirectly, as a parameter of the nonlinear approximation, Hecht equation, to the measured charge amplitude data.

Table 1. Results of the weighted fitting of the CCE data, acquired for different temperatures, to the Hecht equation. The mobility-lifetime product for electrons displays a nonlinear behavior with temperature, while for holes there is an overall decrease in the $\mu\tau$ product with rising temperature. Goodness-of-fit is measured with the R^2 value. Value closer to 1 indicates that a greater proportion of variance is accounted for by the model. Instrumental weighting method was used to incorporate the error of individual data points.

Temperature (°C)	**22**	**98**	**176**	**250**	**337**	**395**	**450**
$\mu\tau$ (electrons) $[(cm^2/V) \cdot 10^{-6}]$	9.3 ± 0.7	8.7 ± 0.7	7.6 ± 0.5	7.2 ± 0.5	8.9 ± 0.6	9.0 ± 0.8	10.1 ± 0.5
R^2	0.973	0.978	0.985	0.973	0.987	0.970	0.989
$\mu\tau$ (electrons) $[(cm^2/V) \cdot 10^{-6}]$	12.9 ± 1.5	10 ± 2	7.8 ± 0.6	6.9 ± 0.5	4.0 ± 0.25	2.6 ± 0.2	1.15 ± 0.06
R^2	0.986	0.992	0.999	0.999	0.986	0.986	0.998

The temperature dependence of the mobility-lifetime product measured for both electrons and holes is presented in figure 10. There is an overall decrease of the $\mu\tau$ value for holes with rising temperature. The rate of decrease is $-2.6 \cdot 10^{-8}\,(cm^2/V)/°C$, obtained from the linear approximation. In absolute values, the $\mu\tau$ product for holes dropped one order of magnitude from room temperature to 450 °C. But, for electrons, small initial decrease, from RT to 250 °C, is reversed at higher temperatures, and it seems that the mu-tau continues recovering to the higher temperatures up to 450 °C, which was the highest temperature covered in this experiment. Decreasing temperature trend of the mu-tau product for both charge carrier types has been observed before in natural diamonds [38]. Continuation of the same trend was observed for high-purity scCVD diamonds in recent measurements for the low temperature region (2K – RT), demonstrating a strong increase in mu-tau with decreasing temperature [39]. However, even though there were other reports of mu-tau performance of high-purity synthetic diamonds at elevated temperatures [13, 40], the systematic study is still missing in the

available literature.

It is expected that carrier's mobility scales with temperature as $\mu \sim T^{-a}$, with $a(T) > 1$ due to scattering on acoustical and optical phonons [7]. This was confirmed for CVD diamonds experimentally for both electrons and holes [41, 42]. Reversal of decreasing trend for mu-tau product, that was extracted from our data, would indicate an improvement of electrons lifetime for temperatures above 250 °C. To try to ratify this theory, we attempted to observe thermally stimulated electron detrapping at these temperatures. More focus was put specially on the sub-microsecond time span, which corresponds to shallow trap level domain (shallow traps are more likely to be present in unintentionally-doped and unirradiated diamond). However, this behavior was not observed, and so we cannot make further conclusions on the possible lifetime increase for electrons. More investigation is needed to confirm these phenomena, preferably by means of direct lifetime measurements in high-purity diamond crystals.

4 Conclusions

Charge transport properties of high purity sc-CVD diamond detector were studied in the temperature range from 23 °C – 450 °C. Ion microbeam was used to induce and spatially map the charge signal in the detector.

Detector region previously exposed to radiation damage, by 5 MeV proton beam, exhibited thermal charge release effect at temperatures above 200 °C. Charge transient spectroscopy was utilized to study the time structure of the output signal transients. Analysis yielded a trap activation energy of 0.53 ± 0.01 eV. This level was only capturing and releasing holes, and it was not detected in the unirradiated detector regions. This indicates that the formation of the deep level occurred during the damaging ion beam irradiation. Existence of this trap in high purity diamond affects the charge transport properties that are important for the possible employment of diamond-based detectors in high temperature and high radiation conditions. However, it needs to be mentioned that electron trapping was also observed after ion beam irradiation, resulting in decreased charge collection efficiency. Thermally stimulated electron releasing was not achieved in the covered temperature span, suggesting that these carriers were trapped by the even deeper defect.

Mobility-lifetime product was also studied separately for holes and electrons in the pristine detector regions. $\mu\tau$ for holes dropped one order of magnitude from room temperature to 450 °C. For electrons, $\mu\tau$ performance varied much less. After the initial decrease, recovery was observed for temperatures above 250 °C, which could be a promising feature of high purity diamond as a semiconductor material for electronic applications at high temperatures.

Acknowledgments

This work was carried out within the framework of the EUROfusion Consortium and has received funding from the 2019-2020 Euratom research and training programs under grant agreement No. 633053.

The authors acknowledge financial support from the European Regional Development Fund project for the 'Center of Excellence for Advanced Materials and Sensing Devices' (Grant No. KK.01.1.1.01.0001) and the IAEA Research Contract F11020.

Data availability statement

The data that support the findings of this study are available upon reasonable request from the authors.

References

1. Tallaire A, Achard J, Silva F, Brinza O, Gicquel A. Growth of large size diamond single crystals by plasma assisted chemical vapour deposition: Recent achievements and remaining challenges. Comptes Rendus Physique. 2013 Feb;14(2-3):169–184. Available from: https://linkinghub.elsevier.com/retrieve/pii/S1631070512001429.

2. Schreck M, Asmussen J, Shikata S, Arnault JC, Fujimori N. Large-area high-quality single crystal diamond. MRS Bulletin. 2014 Jun;39(6):504–510. Available from: http://link.springer.com/10.1557/mrs.2014.96.

3. Wort CJH, Balmer RS. Diamond as an electronic material. Materials Today. 2008 Jan;11(1-2):22–28. Available from: https://linkinghub.elsevier.com/retrieve/pii/S1369702107703498.

4. Pilotti R, Angelone M, Pagano G, Loreti S, Pillon M, Sarto F, et al. Development and high temperature testing by 14 MeV neutron irradiation of single crystal diamond detectors. Journal of Instrumentation. 2016 Jun;11(06):C06008–C06008. Available from: https://iopscience.iop.org/article/10.1088/1748-0221/11/06/C06008.

5. Metcalfe A, Fern GR, Hobson PR, Smith DR, Lefeuvre G, Saenger R. Diamond based detectors for high temperature, high radiation environments. Journal of Instrumentation. 2017 Jan;12(01):C01066–C01066. Available from: https://iopscience.iop.org/article/10.1088/1748-0221/12/01/C01066.

6. Angelone M, Pilotti R, Sarto F, Pillon M, Lecci S, Loreti S, et al. Systematic study of the response of single crystal diamond neutron detectors at high temperature. Journal of Instrumentation. 2020 Mar;15(03):P03031–P03031. Available from: https://iopscience.iop.org/article/10.1088/1748-0221/15/03/P03031.

7. Koizumi S. Power Electronics Device Applications of Diamond Semiconductors. Elsevier; 2018. Available from: https://linkinghub.elsevier.com/retrieve/pii/C20160039992.

8. Iwasaki T, Hoshino Y, Tsuzuki K, Kato H, Makino T, Ogura M, et al. High-Temperature Operation of Diamond Junction Field-Effect Transistors With Lateral p-n Junctions. IEEE Electron Device Letters. 2013 Sep;34(9):1175–1177. Available from: http://ieeexplore.ieee.org/document/6557019/.

9. Kraus B, Steinegger P, Aksenov NV, Dressler R, Eichler R, Griesmayer E, et al. Charge carrier properties of single-crystal CVD diamond up to 473 K. Nuclear Instruments and Methods in Physics Research Section A: Accelerators, Spectrometers, Detectors and Associated Equipment. 2021 Feb;989:164947. Available from: https://linkinghub.elsevier.com/retrieve/pii/S0168900220313449.

10. Steinegger P, Dressler R, Eichler R, Piguet D, Streuli S, Türler A. Diamond detectors for high-temperature transactinide chemistry experiments. Nuclear Instruments and Methods in Physics Research Section A: Accelerators, Spectrometers, Detectors and Associated Equipment. 2017 Apr;850:61–67. Available from: https://linkinghub.elsevier.com/retrieve/pii/S016890021631261X.

11. Kumar A, Kumar A, Topkar A, Das D. Prototyping and performance study of a single crystal diamond detector for operation at high temperatures. Nuclear Instruments and Methods in Physics Research Section A: Accelerators, Spectrometers, Detectors and Associated Equipment. 2017 Jun;858:12–17. Available from: https://linkinghub.elsevier.com/retrieve/pii/S016890021730373X.

12. Ueno K, Tadokoro T, Ueno Y, Sasaki K, Koizumi S, Chayahara A, et al. Heat and radiation resistances of diamond semiconductor in gamma-ray detection. Japanese Journal of Applied Physics. 2019 Oct;58(10):106509. Available from: https://iopscience.iop.org/article/10.7567/1347-4065/ab4044.

13. Tsubota M, Kaneko JH, Miyazaki D, Shimaoka T, Ueno K, Tadokoro T, et al. High-temperature characteristics of charge collection efficiency using single CVD diamond detectors. Nuclear Instruments and Methods in Physics Research Section A: Accelerators, Spectrometers, Detectors and Associated Equipment. 2015 Jul;789:50–56. Available from: https://linkinghub.elsevier.com/retrieve/pii/S0168900215004556.

14. Jansen H. Chemical Vapour Deposition Diamond. 2015 Feb. Available from: https://bonndoc.ulb.uni-bonn.de/xmlui/handle/20.500.11811/6405.

15. Crnjac A, Skukan N, Provatas G, Rodriguez-Ramos M, Pomorski M, Jakšić M. Electronic Properties of a Synthetic Single-Crystal Diamond Exposed to High Temperature and High Radiation. Materials. 2020 May;13(11):2473. Available from: https://www.mdpi.com/1996-1944/13/11/2473.

16. Kramberger G, Cindro V, Mandić I, Mikuž M, Zavrtanik M. Effective trapping time of electrons and holes in different silicon materials irradiated with neutrons, protons and pions. Nuclear Instruments and Methods in Physics Research Section A: Accelerators, Spectrometers, Detectors and Associated Equipment. 2002 Apr;481(1-3):297–305. Available from: https://linkinghub.elsevier.com/retrieve/pii/S0168900201012633.

17. e6 CVD Diamond Book Download;. Available from: https://e6cvd.com/us/diamond-book-download.

18. Bogdanović Radović I. Ruđer Bošković Institute Accelerator Facility. Nuclear Physics News. 2020 Apr;30(2):4–9. Available from: https://www.tandfonline.com/doi/full/10.1080/10619127.2020.1752087.

19. Jakšić M, Bogdanović Radović I, Bogovac M, Desnica V, Fazinić S, Karlušić M, et al. New capabilities of the Zagreb ion microbeam system. Nuclear Instruments and Methods in Physics Research Section B: Beam Interactions with Materials and Atoms. 2007 Jul;260(1):114–118. Available from: https://linkinghub.elsevier.com/retrieve/pii/S0168583X07003515.

20. Cosic D, Bogovac M, Jakšić M. Data acquisition and control system for an evolving nuclear microprobe. Nuclear Instruments and Methods in Physics Research Section B: Beam Interactions with Materials and Atoms. 2019 Jul;451:122–126. Available from: https://linkinghub.elsevier.com/retrieve/pii/S0168583X19303684.

21. Breese MBH, Vittone E, Vizkelethy G, Sellin PJ. A review of ion beam induced charge microscopy. Nuclear Instruments and Methods in Physics Research Section B: Beam Interactions with Materials and Atoms. 2007

Nov;264(2):345–360. Available from: https://linkinghub.elsevier.com/retrieve/pii/S0168583X07015133.

22. Farmer JW, Lamp CD, Meese JM. Charge transient spectroscopy. Applied Physics Letters. 1982 Dec;41(11):1063–1065. Available from: http://aip.scitation.org/doi/10.1063/1.93401.

23. Polyakov VI, Rukovishnikov AI, Rossukanyi NM, Varnin VP, Teremetskaya IG, Druz BL, et al. Charge Transient Spectroscopy Study Of Deep Centers In Cvd Diamond And Diamond-Like Films. MRS Proceedings. 1996;442:687. Available from: http://link.springer.com/10.1557/PROC-442-687.

24. Pehl RH, Goulding FS, Landis DA, Lenzlinger M. Accurate determination of the ionization energy in semiconductor detectors. Nuclear Instruments and Methods. 1968 Feb;59(1):45–55. Available from: https://linkinghub.elsevier.com/retrieve/pii/0029554X6890342X.

25. Pan LS, Kania DR. Diamond: Electronic Properties and Applications. New York, NY: Springer; 2013. OCLC: 1059372868. Available from: https://public.ebookcentral.proquest.com/choice/publicfullrecord.aspx?p=5555237.

26. Ziegler JF, Ziegler MD, Biersack JP. SRIM – The stopping and range of ions in matter (2010). Nuclear Instruments and Methods in Physics Research Section B: Beam Interactions with Materials and Atoms. 2010 Jun;268(11-12):1818–1823. Available from: https://linkinghub.elsevier.com/retrieve/pii/S0168583X10001862.

27. Naaranoja T, Golovleva M, Martikainen L, Berretti M, Österberg K. Space charge polarization in irradiated single crystal CVD diamond. Diamond and Related Materials. 2019 Jun;96:167–175. Available from: https://linkinghub.elsevier.com/retrieve/pii/S0925963518307660.

28. Sato Si, Makino T, Ohshima T, Kamiya T, Kada W, Hanaizumi O, et al. Transient current induced in thin film diamonds by swift heavy ions. Diamond and Related Materials. 2017 May;75:161–168. Available from: https://linkinghub.elsevier.com/retrieve/pii/S0925963516306215.

29. Balducci A, Marinelli M, Milani E, Morgada ME, Prestopino G, Scoccia M, et al. Trapping-detrapping defects in single crystal diamond films grown by chemical vapor deposition. Applied Physics Letters. 2005 Nov;87(22):222101. Available from: http://aip.scitation.org/doi/10.1063/1.2135384.

30. Lohstroh A, Sellin PJ, Wang SG, Davies AW, Parkin JM. Mapping of polarization and detrapping effects in synthetic single crystal chemical vapor deposited diamond by ion beam induced charge imaging. Journal of Applied Physics. 2007 Mar;101(6):063711. Available from: http://aip.scitation.org/doi/10.1063/1.2653669.

31. Shockley W, Read WT. Statistics of the Recombinations of Holes and Electrons. Physical Review. 1952 Sep;87(5):835–842. Available from: https://link.aps.org/doi/10.1103/PhysRev.87.835.

32. Naka N, Fukai K, Handa Y, Akimoto I. Direct measurement via cyclotron resonance of the carrier effective masses in pristine diamond. Physical Review B. 2013 Jul;88(3):035205. Available from: https://link.aps.org/doi/10.1103/PhysRevB.88.035205.

33. Ščajev P, Gudelis V, Ivakin E, Jarašiūnas K. Nonequilibrium carrier dynamics in bulk HPHT diamond at two-photon carrier generation: Nonequilibrium carrier dynamics in bulk HPHT diamond. physica status solidi (a). 2011 Sep;208(9):2067–2072. Available from: http://doi.wiley.com/10.1002/pssa.201100006.

34. Elsherif OS, Vernon-Parry KD, Evans-Freeman JH, May PW. Effect of doping on electronic states in B-doped polycrystalline CVD diamond films. Semiconductor Science and Technology. 2012 Jun;27(6):065019. Available from: https://iopscience.iop.org/article/10.1088/0268-1242/27/6/065019.

35. Pomorski M. Electronic properties of single crystal CVD diamond and its suitability for particle detection in hadron physics experiments. 2008 Aug. Available from: http://inis.iaea.org/Search/search.aspx?orig_q=RN:40093695.

36. Prins JF, Derry TE. Radiation defects and their annealing behaviour in ion-implanted diamonds. Nuclear Instruments and Methods in Physics Research Section B: Beam Interactions with Materials and Atoms. 2000 May;166-167:364–373. Available from: https://linkinghub.elsevier.com/retrieve/pii/S0168583X99011908.

37. Knoll GF. Radiation detection and measurement. 3rd ed. New York: Wiley; 2000.

38. Nava F, Canali C, Artuso M, Gatti E, Manfredi PF, Kozlov SF. Transport Properties of Natural Diamond Used as Nuclear Particle Detector for a Wide Temperatue Range. IEEE Transactions on Nuclear Science. 1979;26(1):308–315. Available from: http://ieeexplore.ieee.org/document/4329650/.

39. Konishi K, Akimoto I, Matsuoka H, Djurberg V, Majdi S, Isberg J, et al. Low-temperature mobility-lifetime product in synthetic diamond. Applied Physics Letters. 2020 Nov;117(21):212102. Available from: http://aip.scitation.org/doi/10.1063/5.0031600.

40. Lohstroh A. Temperature Dependent Charge Transport Studies in Polycrystalline and Single Crystal CVD Diamond Detectors. 2006 Jan. Available from: http://epubs.surrey.ac.uk/id/eprint/855844.

41. Gabrysch M, Majdi S, Twitchen DJ, Isberg J. Electron and hole drift velocity in chemical vapor deposition diamond. Journal of Applied Physics. 2011 Mar;109(6):063719. Available from: http://aip.scitation.org/doi/10.1063/1.3554721.

42. Kato H, Ogura M, Makino T, Takeuchi D, Yamasaki S. N-type control of single-crystal diamond films by ultra-lightly phosphorus doping. Applied Physics Letters. 2016 Oct;109(14):142102. Available from: http://aip.scitation.org/doi/10.1063/1.4964382.